International Journal of Hydrogen Energy 60 (2024) 1392–1403

Contents lists available at ScienceDirect

International Journal of Hydrogen Energy

journal homepage: www.elsevier.com/locate/he

Benchmark of J55 and X56 steels on cracking and corrosion effects under hydrogen salt cavern boundary conditions

Holger Janßen [a,b,*], Luisa Ehmcke [a,c], Barbara Satola [a], Michael Kroener [a], Alexander Dyck [a], Martin Vehse [a], Michael Wark [b], Carsten Agert [a,d]

[a] German Aerospace Center (DLR), Institute of Networked Energy Systems, Carl-von-Ossietzky-Str. 15, 26129, Oldenburg, Germany
[b] Carl von Ossietzky University, School of Mathematics and Science, Institute of Chemistry, Carl-von-Ossietzky-Str. 9-11, 26129, Oldenburg, Germany
[c] Delft University of Technology, Faculty of Mechanical, Maritime and Materials Engineering, Mekelweg 2, 2628 CD, Delft, Netherlands
[d] Carl von Ossietzky University, School of Mathematics and Science, Institute of Physics, Carl-von-Ossietzky-Str. 9-11, 26129, Oldenburg, Germany

ARTICLE INFO

Handling Editor: Prof I Tolj

Keywords:
Hydrogen
Salt cavern
Storage
Hydrogen embrittlement
Crack formation
Steel

ABSTRACT

Salt caverns have great potential to store relevant amounts of hydrogen as part of the energy transition. However, the durability and suitability of commonly used steels for piping in hydrogen salt caverns is still under research. In this work, aging effects focusing on corrosion and cracking patterns of casing steel API 5CT J55 and "H2ready" pipeline steel API 5L X56 were investigated with scanning electron microscopy and energy dispersive X-ray spectroscopy after accelerated stress tests with pressure/temperature cycling under hydrogen salt cavern-like conditions. Compared to dry conditions, significant more corrosion by presence of salt ions was detected. However, compared to X56, only for J55 an intensification of corrosion and cracking at the surface due to hydrogen atmosphere was revealed. Pronounced surface cracks were observed for J55 over the entire samples. Overall, the results strongly suggest that X56 is more resistant than J55 under the conditions of a hydrogen salt cavern.

1. Introduction

The energy transition to renewable energy sources is more urgent than at any time in the past. First and foremost, to counteract climate change with rising temperatures and rising sea levels, but also to become less dependent on other energy-exporting countries. Typical renewable energy sources are photovoltaic and wind energy. The output of both technologies is intermittent and fluctuating, resulting in short-term and seasonal variations [1]. Power generation and demand are not aligned. Accordingly, the development of short-term energy storage is necessary to smoothen the power output to the grid, i.e., to stabilize the frequency, voltage, and power quality of the system. Long-term energy storage between seasons is important to ensure access to reliable energy services throughout the year and to harvest the energy oversupply in the summer, e.g. from photovoltaics (PV). Even during periods of limited sun and wind, typically in the winter time, sufficient energy supply is essential in an electricity-dependent society.

A suitable way to store large amounts of energy over yearly cycles is chemical storage, which is the reason why natural gas has often been used in the past. For an electricity system aiming at climate neutrality, hydrogen (H_2) should replace natural gas and other fossil fuels in many applications. There are several promising research areas and efforts related to H_2, such as various fuel cell powered vehicles [2–4] and environmentally friendly ammonia production [5]. In addition, the steel industry offers great potential for the use of H_2 [6–9]. As the iron and steel industry is responsible for 4% of anthropogenic carbon dioxide (CO_2) emissions in Europe, decarbonization of the sector can contribute significantly to the reduction of greenhouse gases [6,7,9]. As H_2 can be produced in a CO_2-neutral way by electrolysis using renewable energy sources, it supports the idea of the energy transition. However, for a future in which H_2 plays a key role as a secondary energy carrier, the infrastructure for its storage must be implemented. In this field, underground storage in large-scale salt caverns analogous to natural gas has enormous potential. While much experience has already been gained with natural gas storage in salt caverns, there are still unanswered questions to be resolved for H_2 [10]. Due to advantages such as the low porosity of salt rock and the resulting low permeability of hydrogen, the gas tightness of salt caverns has already been proven for

* Corresponding author. German Aerospace Center (DLR), Institute of Networked Energy Systems, Carl-von-Ossietzky-Str. 15, 26129, Oldenburg, Germany.
E-mail address: holger.janssen@dlr.de (H. Janßen).

https://doi.org/10.1016/j.ijhydene.2024.02.168
Received 14 August 2023; Received in revised form 1 February 2024; Accepted 12 February 2024
Available online 28 February 2024

hydrogen [10,11]. In addition, no safety-relevant differences to natural gas are expected with regard to the salt, as it is chemically inert to hydrogen [11]. Nevertheless, there are some challenges of storing hydrogen in salt caverns, such as the economic feasibility (provision of cushion gas to maintain the minimum pressure in the cavity), the quantities of water required for the construction of caverns and the brine (salt concentration) to be disposed of in the process, as well as the challenges discussed here in the study with regard to corrosion and material compatibility. Further issues of life cycle and safety have to be answered [12].

The storage of H_2 in salt caverns has been realized, but is currently not a widely established technology as a secondary energy storage option [13,14]. Therefore, there is limited data on the long-term compatibility of cavern materials in conjunction with H_2. Various materials are needed to build these caverns, including cements, polymers, and steel. This study focuses on steel analyses since steel is extensively utilized for realizing the underground piping of salt caverns. As shown in the next section for some examples, suitable steel grades have been defined for natural gas storage in underground structures, however, the applicability of steels for H_2 storage has yet to be investigated and confirmed. The data presented for steel applications with H_2 in the literature tend to be limited to the class pipeline steels, which are generally used for above ground piping but less for underground piping under the special conditions of salt caverns. Their extended applicability to salt caverns needs to be considered, as this could be a potential new area of interest for these steels. Investigation of the changes in the steel surface under the various salt cavern conditions is the objective of the study presented in this paper.

Pipes used in the industry for various applications are classified and named in accordance with standard technical specifications and nomenclature of the American Petroleum Institute (API). Commercially, casing and pipe steels are used for combined natural gas and underground storage applications. These follow the nomenclature of the class API 5CT with an additional letter/number combination indicating the strength level and determining the grade [15]. Some of the materials in this class have been developed for underground natural gas and oil storage in caverns, such as API 5CT J55 (J55) (weldable) and API 5CT N80 Q (weldable) [16,17].

Boersheim et al. [18] investigated the effects of H_2 on steels typically used in underground storage facilities in Germany, which include API 5CT N80, P110, K55, and J55 casing steels; however, the exact specifications including the material compositions were not published for confidentiality reasons. N80, K55, and J55 were tested for 4 weeks in an autoclave that mimicked the conditions of a cavern containing H_2, but without pressure and temperature cycling. Brine was added to the system, and temperature and pressure were maintained at 100 °C and 100 bar, respectively. In the stress-strain measurements of the steels before and after H_2 exposure, a change in geometry was observed, while hydrogen embrittlement could not be recognized. It should be noted that the time of failure is not indicated in the graphs and the scale was not normalized.

Trautmann et al. [19] investigated the effects of H_2 on API 5CT P110 [15], which is regularly applied in caverns, and on L80, which is used for drilling in acidic environments [18]. The materials were tested for 30 days in an autoclave at 25 and 80 °C with H_2 at partial pressures of 20 and 100 bar, respectively. The omission and addition of an electrolyte represented dry and wet conditions. The results showed that hydrogen uptake increased with elevated temperature, pressure, and combined humid conditions. However, overall hydrogen uptake during testing was low and did not result in failure below the specified minimum yield strength of 90% at constant load.

Another possible steel category for underground storage applications is pipeline steel, which is generally used for oil and gas transportation infrastructure [20]. According to API nomenclature, pipeline steels are classified as API 5L followed by a letter/number combination indicating the strength level and determining the grade [20]. There are some studies on the effects of H_2 on API 5L X70 steel [21–24]. Mohtadi-Bonab et al. [21] studied the steel using scanning electron microscopy (SEM) and other techniques. Polished samples were electrochemically loaded with hydrogen. The effects of the hydrogen were studied microscopically. Two types of damage, blisters and internal cracks, were observed. The number and size of bubbles increased with loading time, reaching up to 1 mm in the 24-h treated sample. The same dependence was observed for internal cracks. Inside the microstructure, structural defects and nonmetallic inclusions served as points of attack. Mohtadi-Bonab et al. [21] used energy dispersive X-ray spectroscopy (EDX) to detect crack initiation and propagation on steel surfaces. They have observed that grain size and microstructure (in)homogeneity influence hydrogen embrittlement. A finer grain structure increases the amount of hydrogen diffusion inhibitors, as grain boundaries with high local concentration of hydrogen can cause structural defects. Nevertheless, further studies are needed, in particular experiments under the boundary conditions of salt caverns, to assess the suitability of X70 steel for use in caverns. Another steel grade commonly used in the European pipeline network is API 5L X52. Capelle et al. [25] showed that hydrogen can penetrate the near-surface layers of the metal even at a pressure of 20 bar and ambient temperature, leading to a change in the local fracture mechanism. It should be noted that the results are valid only for the specific test conditions. Similarly, another study by Boukortt et al. [26] showed hydrogen embrittlement on API 5L X52 through a series of surface cracks near the fracture surface. Because of the hydrogen environment, fracture often occurs near the surface, caused by pitting and hydrogen attack. Occasionally, fracture also begins at secondary cracks.

This work focuses on investigating and discussing the suitability of two steel grades, casing steel API 5CT J55 and pipeline steel API 5L X56 (X56), for potential application in salt caverns for H_2 storage. The motivation for the selection of these steels is explained in the following materials section. Previous studies have often been limited to the theoretical possibility of storing hydrogen in caverns (e.g. gas tightness, microbial activity, utility for the grid) and to the general performance of steels under different hydrogen pressures. However, in this study, particularly the combination of pressurized hydrogen and cavern storage of gases is of interest in the stability analysis of the steels. Therefore, surface investigations with microscopic techniques in combination with surface composition analysis were performed on steel samples after treatment in high pressure reactors with H_2 atmosphere involving variation of temperature, pressure and permanent brine. The objective of the work was to investigate the visible aging effects on the surface, to assign the effects to the applied conditions, and to identify trends in the corrosion and cracking patterns of the steel samples as a function of the exposure conditions and duration.

2. Materials

The API 5CT J55 (Mannesmann Line Pipe GmbH) (Fig. 1a) investigated in this study is a casing pipe steel that is commonly used for natural gas storage in salt caverns, but its application in traditional underground natural gas storage does not automatically qualify it for use in the same with H_2. This steel was normalized during production via a hot rolling mill. The chemical composition of steel grades for casing according API 5CT is mostly comparable and is not subject to major limitations. The differentiation between the 5CT steel grades is based on their properties such as minimum yield strength and tensile strength. The yield strength is also responsible for the grade classification, e.g. for J55 it is 379 MPa [15]. The minimum tensile strength is 517 MPa [15]. Willett [27] investigated the susceptibility of electrically welded J55 to hydrogen-induced cracking (HIC). Extensive HIC was observed during mill testing, which was attributed to segregation in the centerline and inhomogeneity of the microstructure. Although the test setup is not closely related to material testing under H_2 salt cavern boundary conditions, the study shows that hydrogen embrittlement can occur in the material under certain treatments and conditions and therefore testing is

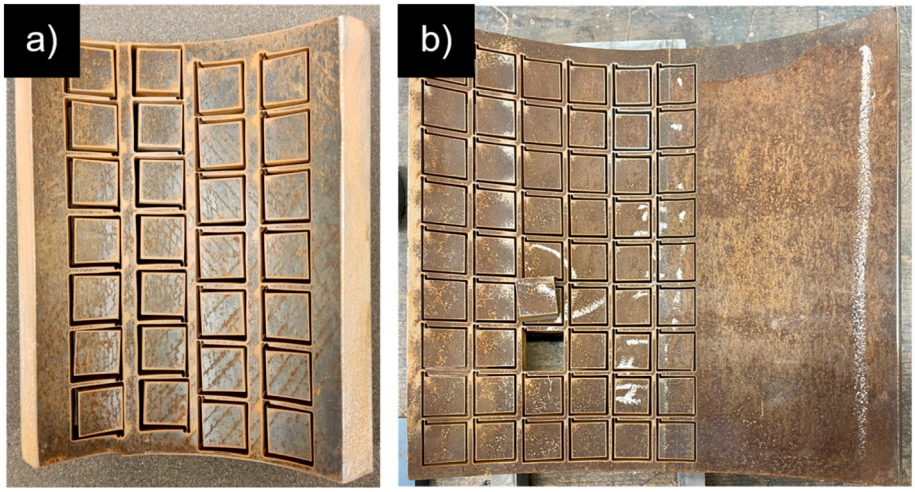

Fig. 1. Pictures of a) API 5CT J55 and b) API 5L X56 after water jet cut prepared samples for accelerated stress testing.

of great importance. In addition, the example shows that special attention should be paid to the welds of the pipelines.

Additionally, the steel grade API 5L X56 (Mannesmann Line Pipe GmbH) (Fig. 1b) was investigated in this study for comparison reasons. This steel follows the "H2ready" production route via thermomechanical rolling of Mannesmann Line Pipe and has a yield strength of 390 MPa and a minimum tensile strength of 490 MPa [20,28]. Although these values are not congruent to the aforementioned API 5CT J55, X56 steel can be produced to meet not only the requirements of X56 steel but also those of J55 steel. Since literature of this relatively new "H2ready" production route is currently only published for the very similar steel API 5L X52 with slightly shifted strength level, this alternative steel grade is used to present the novel steelmaking process and the possible consequences for its suitability for an H_2-storing salt cavern [29]. Brauer et al. [28] investigated two as API 5L X52 classified steels, where steel type 1 was produced using a normalized hot rolling mill and steel type 2 was thermomechanically rolled according to Mannesmann Line Pipe specifications for "H2ready" pipe. Steel type 2 was found to have increased grain refinement and higher homogenization rate compared to steel type 1. Slow strain rate tests (SSRT) conducted in an 80 bar H_2 environment indicate that steel type 1 is affected by H_2, while steel type 2 demonstrates good resistance to H_2-induced degradation. Since H_2 dissociates on active metal surfaces (free of oxide layers), their formation should be avoided by reducing the occurrence of notches and ridges inside the tube. Moreover, the reduction of active metal surfaces suppresses local stress fields and thus critical crack growth. The results of the presented study [28] refer to the application in pipelines. A test under the boundary conditions of salt caverns was not performed in the referred study. To improve the resistance to hydrogen embrittlement, the chemical composition of the alloy plays an important role [26,30,31]. A lower carbon content improves weldability and thus reduces the probability of hydrogen penetration into the alloy. Reducing the phosphorus and sulfur content minimizes the material's points of attack due to lower impurities. Another important factor in durability is microstructure, which can be affected by the manufacturing process. For this, no independent studies were identified.

Since the "H2ready" production route seems to be promising for the production of H_2-resistant steels, in this presented study, the aforementioned API 5L X56 (X56) pipeline steel was selected for the investigations in addition to the conventional casing steel J55. The research question does not refer to the general applicability for H_2, but to the suitability under salt cavern boundary conditions in combination with H_2. Surface tests were performed and the results of the two steels were compared. It should be remarked that within the classification according to API 5CT J55 or API 5L X56 the mentioned properties regarding strengths or limits in the chemical composition are prescribed, but due to the different manufacturing processes (as described for "H2ready" X56) or slightly different chemical compositions there may be differences regarding the qualification for caverns and pipelines for hydrogen.

2.1. Microstructural analysis of J55 and X56

For the evaluation of SEM images, knowledge of the microstructure is helpful for further interpretation. Grain boundaries, interstitial sites and impurities can play a decisive role, especially in the interaction of H_2 and the investigated steels [30–32]. In the later part of this paper, the microstructure will be used for discussion. The images shown in Fig. 2 represent the microstructure with marked grain boundaries of the two steels studied, J55 and X56. The structure was obtained after polishing the surface to 0.25 μm and subsequent etching with 3 vol% Nital (3 vol% nitric acid (Roth ROTIPURAN®, purity ≥65%) in ethanol (Roth ROTIPURAN®, purity ≥99.8%)). Grain size was determined by averaging the length of several grains in multiple directions. For this, 300 length measurements per sample were performed using the image processing software ImageJ and the average of three samples per steel was determined.

Analyzing three different images for J55, a mixture of pearlite and ferrite can be determined after visual comparison with images from literature [16,33,34]. The average grain size was measured to be 6.60 ± 2.62 μm. For X56, a major ferrite structure with a reduced fraction of isolated pearlite grains can be identified by comparing images from literature [35,36]. Clover et al. [37] confirmed this structure in their study on X56. An average grain size of 3.57 ± 1.74 μm was determined.

3. Methods

3.1. Sample preparation

Samples of the two steels J55 and X56 were cut out of steel pipes by water jet cutting in squares of 20 mm × 20 mm with a thickness of 19 mm for J55 and 13 mm for X56, respectively. The chemical stability of the steel types was investigated comparing untreated and sanded sample surfaces. The sanding was conducted in order to induce crack formation, enlarge the (active) surface area and increase probability for hydrogen uptake. Only the four cutting surfaces were sanded to maintain the curvature and coating of the samples. The samples were sanded with a sanding machine (LaboPol-20, Struers GmbH) using a resin bonded diamond disc (MD Piano 220) with a hardness classification of HV 220. Subsequently, the sanded samples were washed twice for 2 min each in

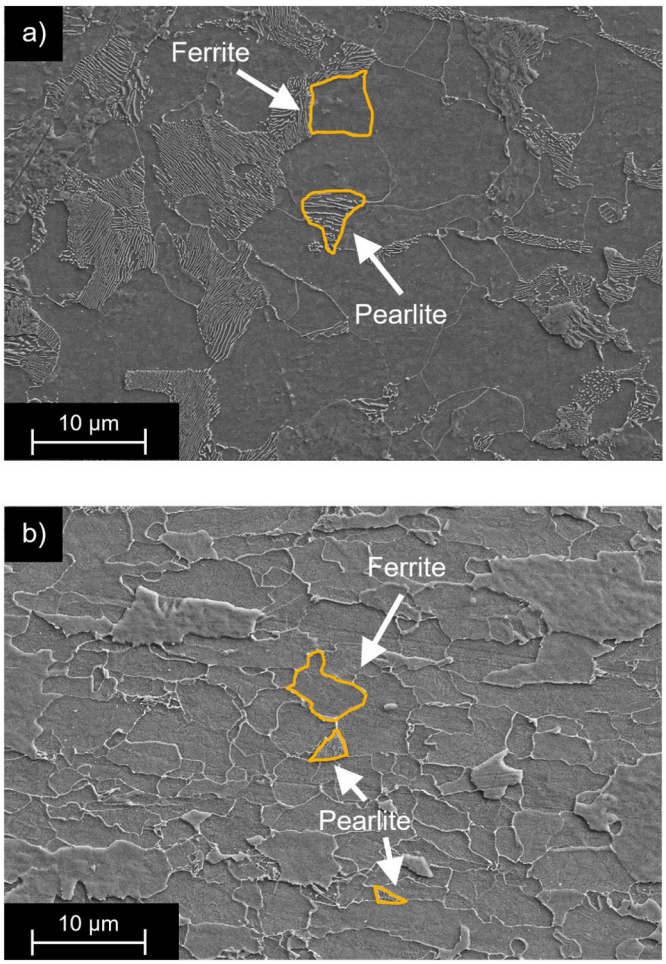

Fig. 2. Microstructure SEM image of a) API 5CT J55 and b) API 5L X56 after polishing to 0.25 µm and subsequent treatment with 3 vol% Nital etch.

fresh isopropanol (Roth 2-Propanol, purity 99.5%) in the ultrasonic bath (Elmasonic S10H).

3.2. High-pressure reactor

The accelerated stress test experiments were conducted in order to investigate the impact of salt cavern boundary conditions on different steels. The experiments were performed in high-pressure reactors (BR-500, Berghof Products + Instruments GmbH) containing a 316Ti stainless steel cylinder with an inner PTFE cylinder with a liquid volume of 500 mL.

The selection of variations in the experiments is shown in Fig. 3. For both materials, 12 experiments were performed in total derived from a combination of the initial sample conditions (untreated or sanded), the reactor conditions (dry, water and brine), and the gases used (H_2 and nitrogen (N_2)). Each test was conducted with a new sample. First the sample was placed in the PTFE cylinder. Subsequently, the reactor chamber was purged with 100 bar gas pressure. As the respective process gases H_2 (Linde GmbH, purity 6.0 (>99.9999 %)) or N_2 (Linde GmbH, purity 6.0 (>99.9999 %)) were used. Measuring the oxygen (O_2) and N_2 content of the gas in the reactor, the required number of 6 purging cycles was determined in order to have a concentration of over 99.999 % for H_2 in the reactor at the start of the test. For accelerated ageing temperature cycling was performed. Starting at room temperature (approx. 25 °C) the temperature was cycled between 160 °C and −10 °C (process thermostat "Grande Fleur", Peter Huber Kältemaschinenbau AG). Simultaneously, pressure cycling between 90 and 150 bar was induced as a consequence of the temperature cycling within the reactor. Heating and cooling were conducted repeatedly in six cycles and the set temperatures were hold constantly for 4 h each time resulting in 72 h (3 days) in total. Then, the measurement was stopped at 25 °C. The sample was removed from the chamber, rinsed with isopropanol (Roth 2-Propanol, purity ≥99.5 %) and dried with a N_2 gas gun. Besides this "dry" condition, the same experiments were also performed using two different types of liquid (20 mL) within the chamber. In the "water" condition experiments high-purity water ($\rho \geq$ 18,2 MΩ/cm) was used. And for the "brine" condition artificially recreated brine was prepared and applied in the chamber which was based on a measured composition of a brine extracted from a salt cavern. The brine was mainly composed of Na^+ ($c = 5.513\ mol/L$) and Cl^- ($c = 5.442\ mol/L$) ions and additionally contained K^+ ($c = 14\ mmol/L$), Mg^{2+} ($c = 10\ mmol/L$), Ca^{2+} ($c = 24\ mmol/L$), SO_4^{2-} ($c = 42\ mmol/L$) and Br^- ($c = 0.3\ mmol/L$) ions as minor constituents. The samples were immersed in the liquids during the experiments. Furthermore, in addition to the 3 days cycling, 14 days cycling was performed with selected environments using only dry and brine conditions with H_2. Thus, additional 4 samples per steel type result from these combinations.

3.3. Scanning electron microscopy and energy dispersive X-ray spectroscopy

The samples were analyzed with a scanning electron microscope and an energy dispersive X-ray spectroscope (ZEISS NEON 40 EsB). An accelerated voltage of 15 kV was used for the measurements. The surfaces were screened for pits and cracks with a magnification of 200X. The EDX analysis was performed with a 35X magnification at three random spots in order to calculate a mean value for the weight percentage of the detected elements. For the reference three pristine

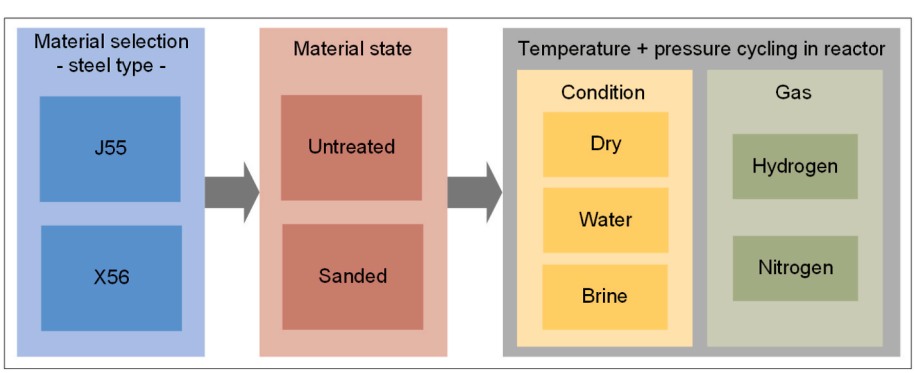

Fig. 3. Overview of experiments performed with two different steel types. Surface state prior to the experiment start and varied conditions in the high-pressure reactor to emulate a hydrogen filled salt cavern and comparative measurements with defined environments are shown. Each experiment is the varied combination of the individual boxes (e.g. J55, sanded, brine, hydrogen).

samples were analyzed and the mean values were calculated.

4. Results and discussion

In the following results, the influence of H_2 storage under cavern conditions on casing and pipeline steels is considered via accelerated stress tests. To determine the various influencing factors, different conditions in the reactor (dry, water, brine, each with H_2 and N_2), steel types (J55 and X56) and experiment durations (3 and 14 days) were applied as described in the methods section. The temperature and pressure thresholds of the cycling were not varied between experiments. After first discussing the results of the corrosion resistance determined by EDX, the results of the SEM investigation follow.

4.1. Analysis of corrosion with energy dispersive X-ray spectroscopy

The following figures focus on the discussion of elements most significant for corrosion, which are iron (Fe) and oxygen (O). Other elements detected in the EDX were mainly carbon and are not shown in the following diagrams for a better overview. The proportion of the two elements Fe and O on the surface is shown as a function of the conditions investigated. In red the proportions of Fe are shown, in blue those of O. The reference values (half-filled triangles) were determined by averaging 3 different steel samples without any exposure to experimental conditions in the reactor. The filled symbols refer to the 3 days tests, the empty ones to 14 days tests. The squares show the values for high pressure experiments under H_2 atmosphere, the circles those under N_2 atmosphere. The graphs were divided into untreated and sanded samples to make it simpler to interpret the results when the initial conditions are the same. This results in two figures for each material (J55 and X56).

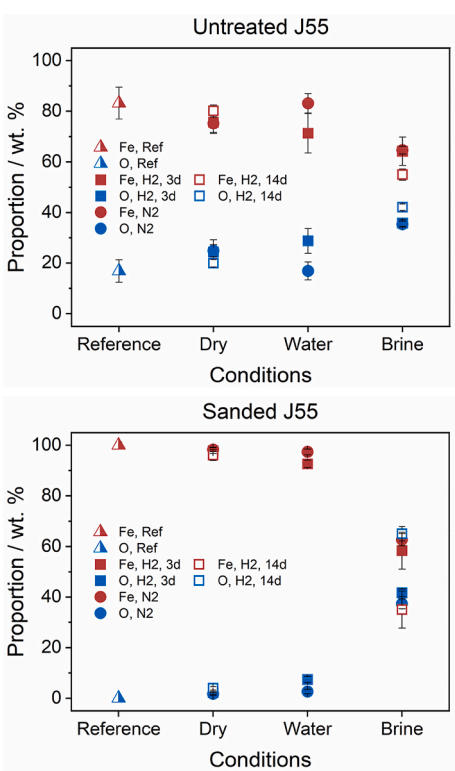

Fig. 4. Results from EDX analysis for Fe and O on untreated and sanded surfaces of J55 samples before (reference) and after 3 days (3d) and 14 days (14d) of high-pressure experiments. Visualized are results from varied conditions (dry, water, brine) and gases (H_2, N_2).

4.1.1. EDX analysis of J55

Fig. 4 shows the EDX results of the corrosion determination for casing steel J55. In general, it can be seen that at the end of the experiments, the Fe content is smaller compared to the reference, while the O content is larger. This is a clear indication that under all conditions (except for the sample untreated, water, N_2, 3 days) corrosion has taken place via the formation of iron oxide. Since the off-trend sample was not analyzed by EDX prior to the test, this result is considered as an exception.

In the following, the individual applied conditions in the reactor will be compared. It can be seen that less iron oxide was formed under dry condition for both sample states than under water and brine conditions. This is in line with expectations, since high-purity gases (H_2 6.0 and N_2 6.0, both with purity >99.9999%) were used for the experiments containing only small traces of O_2 and water. Thus, corrosion at the surface is only limitedly probable. Nevertheless, it is possible that the reactor was not sufficiently purged of atmospheric O_2 despite the purging processes with the investigated gases (H_2 or N_2) before the start of the experiment. The aim was to achieve an O_2 content similar to that of H_2 5.0 (purity >99.999%) prior to the experiment. However, contamination with O_2 and water cannot be precluded.

Compared to the dry conditions, the experiments under water and brine conditions show significantly more iron oxide formation. This effect is particularly pronounced for the sanded samples, since surface oxides were removed when the reference was sanded before the start of the experiment and thus no oxygen was determined. This result illustrates that corrosion is generally promoted by moisture. Corrosion of iron in combination with water is possible via several reaction steps. Due to the high-purity water ($\rho \geq 18.2$ MΩcm) or brine used, an alkaline cathodic reaction of water is likely (the products are hydroxide ions), while Fe ions are formed via anodic dissolution of Fe. Iron hydroxide ($Fe(OH)_2$) is formed from the two intermediate products, and further reaction is possible under alkaline conditions to form hematite ($Fe_2O_3{*}H_2O$) [38]. However, it is beyond the scope of this work to isolate and determine the iron oxide products.

The results for J55 are to be compared for water and brine condition, since the latter corresponds to the conditions of the salt cavern, especially in combination with H_2. Fig. 4 shows that more iron oxide is formed for the brine condition than in ultrapure water. This is particularly striking for the sanded samples. The difference in the corrosion rate can be explained by the presence of different salt ions. The composition of the brine was explained in the methods section. The effects of three metal ions from the salts (sodium (Na^+), magnesium (Mg^{2+}) and calcium (Ca^{2+}) with chloride (Cl^-) as anion) on N80 were studied by Lin et al. [17]. N80 is another casing steel grade within the API 5CT classification. A decrease in corrosion rate with increasing ion concentration was observed for Na^+. This trend was attributed to the reduction in oxygen dissolution by the Na^+ ions [17]. For Mg^{2+}, a radical increase in corrosion rate was observed due to acceleration of ion transport in the salt solution. Ca^{2+} showed suppression of corrosion at low concentrations, but above about 30 wt % it showed enhancement due to dynamic formation of Ca deposits by Ca precipitation [17]. The results of this study can be directly applied to the J55, since oxygen dissolution and ion transport depend on the solution and not on the steel.

Elfergani and Abdalla [39] studied the effect of chloride (Cl^-) concentrations on the corrosion rate with different ASTM A285 grade C carbon steels [40]. The Cl^- concentration was regulated from 1 to 6 wt % by the addition of NaCl, which led to a corresponding increase in the Na^+ ion concentration. A maximum in the corrosion rate was found at 3 wt % NaCl. The maximum can be explained as an equilibrium state between the corrosion acceleration by Cl^- and the mentioned corrosion suppression by Na^+. In any case, the Cl^- has an intensifying effect on corrosion. Firstly, it has the ability to penetrate the passivating iron oxide layer, leading to destabilization and localized corrosion attack. Secondly, it catalyzes the anodic reaction of Fe to Fe(II) [39]. Zhao et al. also described a possible catalytic mechanism that accelerates the

corrosion reaction by Cl^- [41]. Kasthuri et al. [42] demonstrated similar effects of NaCl, namely an initial increase in the corrosion rate with increasing Na^+ concentrations followed by a decrease. The results shown can be applied to the J55 studied here, since the chemistry of the passive layer and the catalytic reactions might be similar.

While some salt compounds enhance corrosion, others have a reducing effect, such as suppressing oxygen dissolution. Therefore, varying chemical compositions of the brine in different salt caverns can have different effects on the steel. The simulated salt solution prepared and used here on the basis of a real brine sample shows an overall intensification of corrosion.

A further trend emerges when comparing the tests under H_2 and N_2 at the same conditions in each case (water or brine). As N_2 (inert) can only have limited negative effects on corrosion due to the high pressure but not due to chemical reactions by the gas molecules, corrosion is slightly pronounced under H_2 atmosphere, as expected. Thomas et al. [43] were able to show an enhancement of the corrosion effects for Fe with absorbed H as well as for different types of steels. The enhancement could be attributed to various effects of H_2 on the steel and its passivation layer. Local phase transformations may occur due to the enrichment of the metal lattice [44]. In addition, various postulations claim that H_2 could cause destabilization of the passivation layer. It is assumed that H_2 reduces oxygen, the passive film, and oxygen-containing species such as O^{2-} and OH^- within the passive film [45–47]. These reduction processes change the chemical composition of the passive film, altering its electronic properties and stability [48]. While this theory could explain the increase in corrosion in the untreated samples, the sanded samples do not exhibit a passive film on the surfaces studied. However, Thomas et al. also showed that in steel with absorbed hydrogen, hydrogen intrinsically enhances the anodic reaction (iron dissolution) [49]. Weakening of local metallic bonding by interstitial H-atoms was shown [43]. The combination of the proposed mechanism, destabilization of the passive layer and promotion of iron dissolution, could change the chemical composition of the passive layer such that more O and less Fe would be present. In the EDX results this is only evident for untreated/sanded and water condition. Considering the error bars, for the other conditions these differences are not emphasized. However, the EDX technique is not sensitive enough for such observations and various other mechanisms and reactions add to the complexity. Although the trend visible in this study cannot be definitively assigned to any of the above theories, hydrogen appears to enhance corrosion. Since the trend is observed not only in the untreated samples but also in the sanded samples, this is an indicator for the promotion of Fe dissolution.

For accelerated stress testing of the above discusses results, an experiment duration of 3 days with temperature (and pressure) cycling was specified. In order to be able to estimate the long-term effects of storing H_2 in salt caverns as a function of the steels tested, 14 days experiments were carried out under H_2 atmosphere for the conditions of particular interest. The results of the tests are shown as empty squares for untreated and sanded, and for dry and brine conditions in Fig. 4. Generally, it can be seen that, with the exception of untreated dry condition, the oxygen content is higher and the iron content lower after 14 days than after 3 days, as expected. This is a clear indication that significant further corrosion occurs between 3 and 14 days and that there was no saturation with iron oxide after 3 days of accelerated stress testing on the surface. The sample not following the trend is considered to be an anomaly, since irregularities in the original oxide layer cannot be excluded, especially in the untreated samples, so that other reference values would be necessary.

4.1.2. EDX analysis of X56

The results demonstrated in the following consider a pipeline steel of a newer type, which is supposed to be particularly stable for H_2 applications due to its homogenized surface ("H2ready"), but which has not yet been tested for salt cavern use.

In Fig. 5, the results of the corrosion study of the X56 steel samples

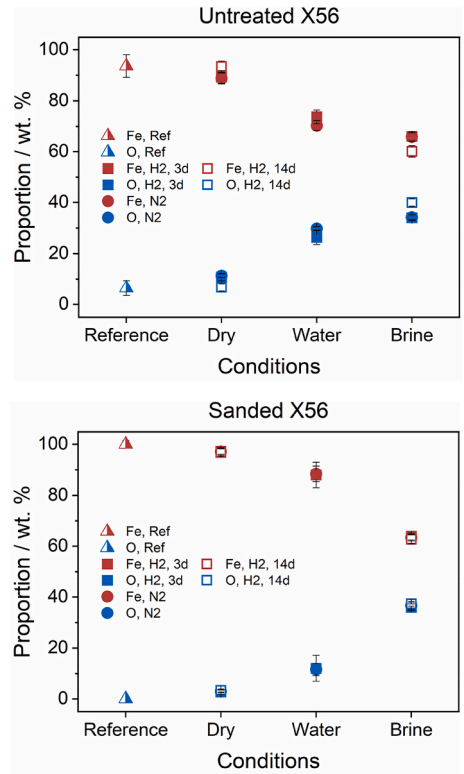

Fig. 5. Results from EDX analysis for Fe and O on untreated and sanded surfaces of X56 samples before (reference) and after 3 days (3d) and 14 days (14d) high-pressure experiments. Visualized are results from varied conditions (dry, water, brine) and gases (H_2, N_2).

under different conditions (dry, water, brine and H_2, N_2) for 3 and 14 days are compared with the reference. The color code corresponds to that of Fig. 4 for the J55 steel. In general, the trend shows again a decrease for the Fe content and an increase in the O content from reference to dry, water, and brine environment. Thus, this repeatedly indicates surface corrosion. Under dry conditions, only a very slight difference can be seen between the tests with H_2 and N_2, so that the assumption of the presence of small residual amounts of water and oxygen in the respective reactor during the test continues to explain the corrosion that has taken place. Since the X56 steel investigated here largely corresponds to the specifications of J55 in terms of chemical composition and strength level, the corrosion rates under water and brine conditions are as expected higher than under dry condition. It is also evident for X56 that the cathodic adsorption of oxygen and the anodic release of iron can cause iron hydroxide and consequently further iron oxides to form on the surface. More detailed explanations were discussed in the previous section on J55.

4.1.3. Comparison of EDX results for J55 and X56

To highlight the differences in terms of corrosion between the two studied steels under cavern conditions, Fig. 6 summarizes the particularly interesting results with sanded samples and brine conditions from Figs. 4 and 5. The proportion of Fe and O on the surface is shown as a function of the gases studied and the experiment duration. Again, in red the proportions of Fe are shown, in blue those of O. The stars refer to J55, the triangles to X56. The reference values are represented as half-filled symbols.

By comparing the results for sanded X56 samples under brine conditions for 3 days for H_2 exposed samples to those for N_2 exposed ones, in contrast to J55, no significant deviations in the Fe and O contents are apparent. The same was found for the water conditions (Fig. 5), but is particularly noteworthy for the experiments under brine condition and

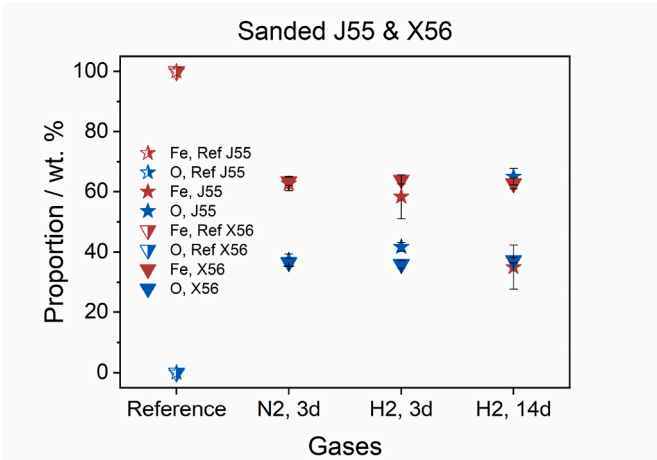

Fig. 6. Compared results from EDX analysis for Fe and O on sanded surfaces of J55 and X56 samples before (reference) and after 3 days (N_2 and H_2) and 14 days (H_2) high-pressure experiments under salt cavern conditions (brine).

thus the most cavern-like condition. This difference to J55 is an important observation as it indicates that X56 has a higher resistance to H_2 due to the lower corrosion rate under H_2 atmosphere and thus seems more suitable for potential use in a H_2 cavern.

The "H2ready" production route of Mannesmann Line Pipe GmbH, which was applied for X56, uses a lower phosphorus and sulfur content in the alloy reducing impurities and thus the points of attack for hydrogen atoms. Furthermore, this route results in grain refinement and homogenization of the steel structure, especially from the surface. This was confirmed by analyses of the microstructures carried out for J55 and X56 (Fig. 2) showing finer grains for X56 (3.57 ± 1.74 μm) than for the J55 steel (6.60 ± 2.62 μm) and a more homogeneous distribution at the surface. In addition, only isolated pearlite grains are visible in X56, while in J55 there is a clearly evident mixture of ferrite and pearlite grains (Fig. 2). Various studies using thermal desorption spectroscopy (TDS) and hydrogen desorption energy calculations have shown that grain boundaries can act as relatively strong hydrogen trap sites [50–52]. In consequence, the altered microstructure with finer grains for X56 reduces hydrogen trapping in the material. As discussed for the J55 steel, it has been postulated that trapped hydrogen increases the probability of iron dissolution by reducing the metallic bond strength near the trapped hydrogen. Since an increase in iron dissolution enhances corrosion effects, trapping hydrogen could be directly related to increased corrosion. Consequently, if the material treatment reduces the trapping potential for hydrogen, it also reduces the corrosion-promoting effect of hydrogen. Although there is no clear difference between the samples exposed to H_2 and the N_2 equivalents, it cannot be ruled out that the H_2 has some influence on corrosion that is not visible within the sensitivity of the characterization method used.

The results of the 14 days tests of X56 for the untreated sample are very comparable to those of J55, but for the sanded sample of X56 a significant difference to J55 can be seen (Fig. 6). While this is only marginally apparent for the sample under dry condition (Figs. 4 and 5), the difference under brine condition (Fig. 6) is much more pronounced. For J55, after 14 days under this condition, there was a significantly lower Fe content on the surface than after 3 days and a correspondingly higher content of O. For X56, the Fe and O contents are even within the error bars of the 3 days test. Based on these measurements, it is reasonable to conclude that in the case of accelerated stress testing, a passivating (bulk material protecting) entire iron oxide layer has already formed after 3 days and therefore no further corrosion products can be detected after 14 days. Thus, the long-term results also confirm the statement that this "H2ready" X56 appears to be better suited under the cavern conditions and that the manufacturing process has a positive effect regarding the cavern conditions simulated here under accelerated stress testing.

4.2. Surface crack analysis with SEM

The microscopic investigation is intended to identify the trends in surface features such as surface cracks and fractures in the two steel types. As in the previous section, all conditions (dry, water, brine and H_2, N_2) and steel types in both states (J55: untreated, sanded; X56: untreated, sanded) were analyzed, but in the following section only images of selected samples are shown, e.g. after treatment under the most extreme conditions. Several potential cracking variants exist and were observed, e.g. corrosion fatigue (CF) or several types of environmentally induced cracking (EIC) such as stress corrosion cracking (SCC), hydrogen induced cracking (HIC) and stress-oriented hydrogen induced cracking (SOHIC).

4.2.1. SEM imaging for J55

In the following part, the cracking and the consequences for the J55 steel will be considered first. For comparison, Fig. 7 shows the sanded reference sample J55 before performing the experiments in the high-pressure reactors. Fig. 8 shows two images of J55 at 200X magnification after the end of the experiment with sanded sample a) after 3 days and b) after 14 days of experiment, both under brine conditions and H_2 atmosphere. First of all, it can be seen that in the reference sample (Fig. 7) only the marks of sanding and no initial cracks are visible. After 3 days of accelerated stress test, some cracks are already present on the surface of the sample, which are branched and discontinuous to some extent, as shown in the three magnified areas. A representative selection was chosen here. Comparable crack formation patterns can be found on the entire surface. The formation of cracks in local corrosion features on the surface can be seen. The same crack patterns apply to the sample after 14 days, but occurrence is much more pronounced. Here, distinct cracks can already be seen without additional magnification, which often develop in a branched manner. After 14 days, the cracks grow through the entire surface, which was not the case after 3 days of stress test. From these observations it can be concluded that the cracks grow with time of exposure and additional cracking takes place. Therefore, the material suffers from prolonged exposure to the salt cavern conditions.

Possible cracking variants are discussed in the following. HIC typically exhibits straight-line regular cracking without branching, so this process is not applicable in the case of J55 [53]. SOHIC is caused by hydrogen absorption followed by internal recombination and can be initiated by HIC and SCC [53,54]. SOHIC is typically observed next to welds in the heat affected zone and exhibits a ladder-like crack array without much branching [54]. Since Fig. 8 shows a very branched pattern without a clear perpendicular or laminar continuation of the

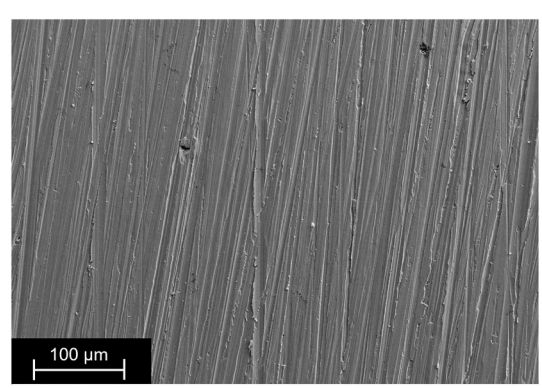

Fig. 7. SEM image of the sanded reference sample J55 at magnification of 200X.

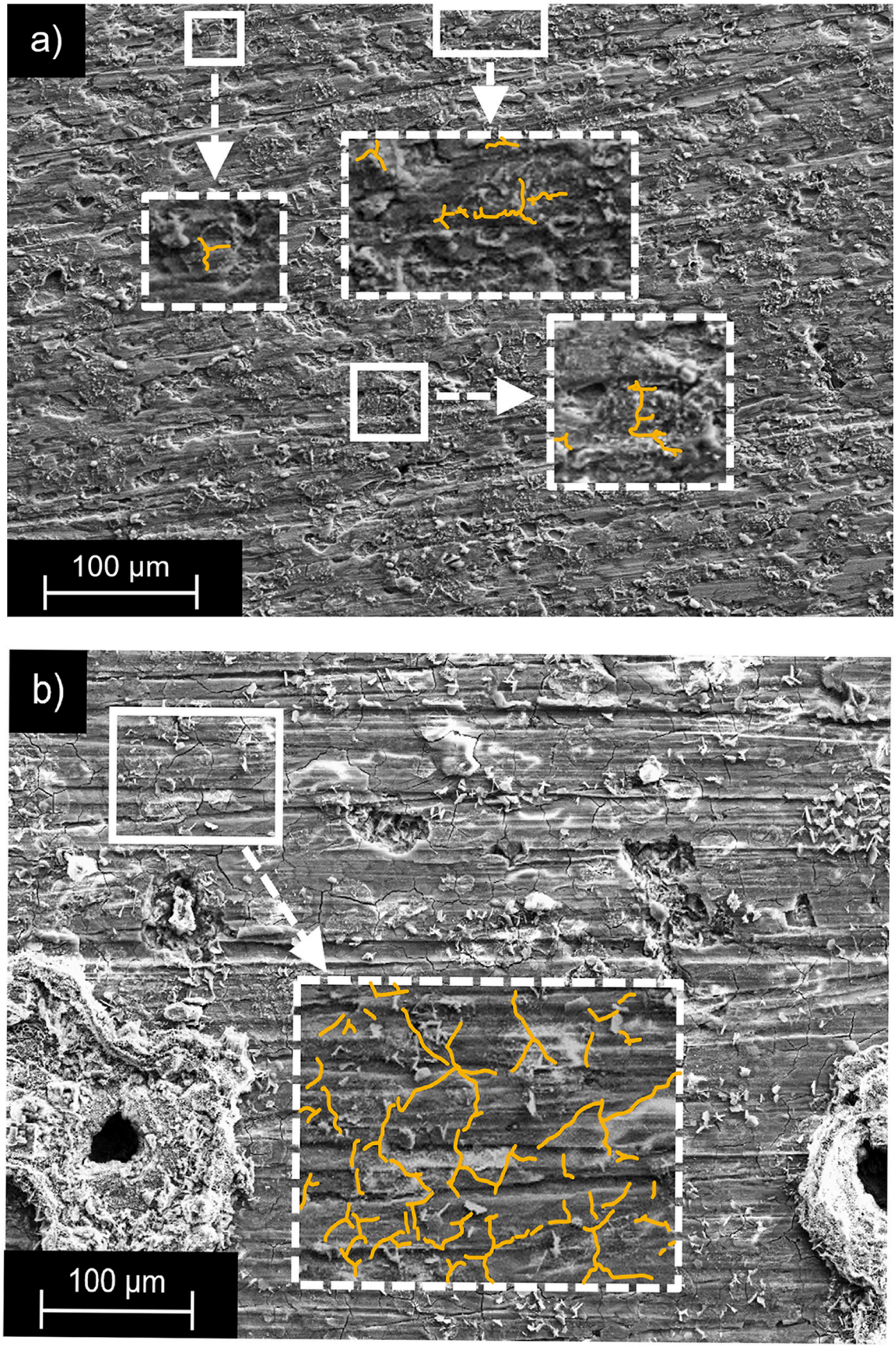

Fig. 8. SEM images of sanded J55 samples at magnification of 200X after a) 3 days and b) 14 days high-pressure experiments with H_2 and brine. In the images, the cracking patterns in the marked areas (continuous line) are highlighted in yellow within the magnification of these areas (dashed line). (For interpretation of the references to color in this figure legend, the reader is referred to the Web version of this article.)

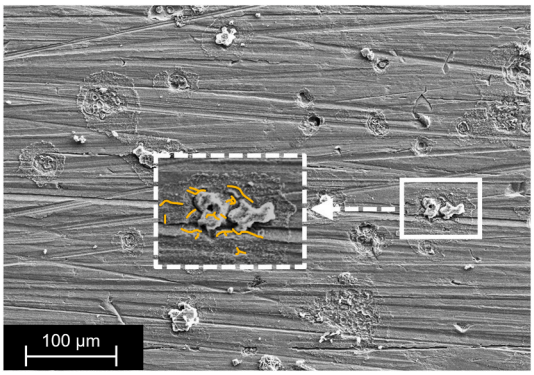

Fig. 9. SEM image of sanded J55 samples at magnification of 200X after 3 days high-pressure experiments with N_2 and brine. In the images, the cracking patterns in the marked areas (continuous line) are highlighted in yellow within the magnification of these areas (dashed line). (For interpretation of the references to color in this figure legend, the reader is referred to the Web version of this article.)

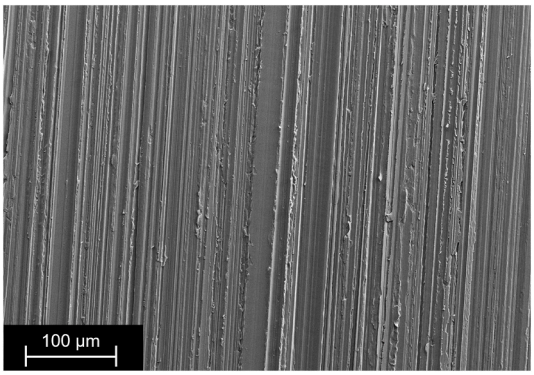

Fig. 10. SEM image of the sanded reference sample X56 at magnification of 200X.

cracks and the cracking is also observed in SEM images after N_2 exposure (Fig. 9), HIC and SOHIC can be excluded as the main cracking mechanisms. The highly branched cracks typical of SCC coincide with the visible cracks (Fig. 8), however, SCC exhibits a striking feature of little corrosion on the stress corrosion surface even in a corrosive solution [53]. This distinguishing feature does not fully apply here, since the EDX results indicate the presence of small amounts of corrosion products (iron oxide) in the crack structures, although less oxygen is found in these locations than in the surrounding areas. While the environmentally induced cracking variants do not evidently qualify as the main cracking mechanism, CF could be the underlying factor. CF combines a corrosive environment (brine) with cyclic stresses that can be caused by temperature and hydrogen-independent pressure cycling. Corrosion products within the cracks as well as a barely present branching are characteristic features [53]. Crack formation often starts in pit-like structures or local oxide particles for J55, which is consistent with the CF theory. However, branching is visible in the crack structures, which contradicts this theory. As mentioned earlier, several cracking mechanisms can occur simultaneously, so differentiation and definite assignment is limited with the applied characterization methods [53]. Based on the experimental conditions and some visible features, CF probably plays an important role in the cracking process of the steel samples. In the brine, more localized corrosion attacks may occur due to the salt ions, thus providing more trigger points for CF.

Comparing the samples in environments with N_2 exposure (Fig. 9) with those in H_2 exposure (Fig. 8), an increase in crack occurrence is observed with H_2. Additionally, it is evident that cracking occurs over a wider area, and is less limited to a specific surface feature and single oxide structures. However, the morphologies of the H_2 exposed samples may be dominated by fatigue cracking as well as CF, possibly in combination with SCC or hydrogen-assisted cracking (HAC). Hydrogen atoms could be absorbed and accumulate in the crack tip, accelerating further cracking. In the hydrogen-enhanced decohesion (HEDE) theory, crack propagation and acceleration are explained by the decreased binding energy of the lattice caused by the agglomeration of hydrogen atoms at the crack tip [55]. This is an explanation for the increase in crack formation under H_2 atmosphere. It should be noted that exposure to H_2 also led to an intensification of corrosion effects in J55, increasing the initiation points for crack formation and thus the crack frequency.

4.2.2. SEM imaging for X56

To further extend and, where appropriate, confirm the conclusions from the EDX observations regarding the suitability of J55 and X56 for use under cavern conditions, the SEM images of X56 are presented below and compared with those of J55.

The images of X56 at 200X magnification are shown with the sanded reference sample in Fig. 10, and with the sanded samples under brine condition and H_2 atmosphere after 3 days (a) and after 14 days (b) of experiment in Fig. 11. After 3 days, as with J55, some cracks and deposits can be located distributed over the surface, but the frequency of these cracks is rather limited. The entire surface of the sample must be scanned to find individual sections with single cracks. The same applies to the sample after 14 days of exposure. Similarly, to the 3 days results, a homogeneous oxide structure with some oxide containing holes is found (via EDX mapping of oxygen) on the surface with only a few short and less branched cracks. However, it can also be seen that, as with J55, these cracks start in pits and grow from there. Local corrosion promoted by salt ions creates stress concentration points and consequently initiation points for crack formation. As mentioned earlier, in the CF mechanism, local corrosion points, such as pits, often serve as initiation points [53]. As far as cracking is concerned, only a few differences between the 3 days and 14 days tests can be identified (Fig. 11).

By comparing the SEM images of H_2 and N_2 exposed samples (Figs. 11 and 12), it is apparent that, unlike the J55 sample, there is no clear deviation in the frequency of cracks. As described previously, the microstructure of the steel affects the hydrogen diffusivity. Grain boundaries with strong hydrogen trap sites (high local concentration of hydrogen) can cause structural defects, so that a finer grain structure increases the amount of hydrogen diffusion inhibitors (less hydrogen trapping) [50–52]. It is not only the finer and more homogeneous grain boundaries in the microstructures that have an influence in detail, but also the general ratio of ferrite and pearlite structures. Steels with a higher pearlite proportion are more susceptible to HIC and SCC [35,56,57]. The images show that the finer and more homogeneous grain structure of X56 reduces the negative impact of H_2. According to the described HEDE theory, the prevention of hydrogen trapping is of great importance, since in consequence HIC, HAC as well as SOHIC cannot occur.

The comparison of sanded X56 (Fig. 11b) and J55 (Fig. 8b) samples after 14 days of exposure to H_2 and brine condition reveals, firstly, a much more homogeneous oxide layer and, secondly, reduced cracking in frequency and severity for X56. Iron oxide can serve as a natural protective layer if uniform corrosion is present on the surface and is not a general indication of loss of material strength. The surface of J55 appeared rough and with various localized attack points in SEM images. Localized corrosion leads to stress concentration factors that reduce rather than increase the strength and durability of the steel. However, the EDX results in the previous section also displayed an effect of H_2 on the corrosion rate for J55, suggesting that additional reactions are involved besides natural oxide formation. As discussed earlier, hydrogen could change the composition of the oxide layer by reducing oxygen species in the layer and catalyzing iron dissolution. Changes in chemical composition can lead to changes in both electronic properties and

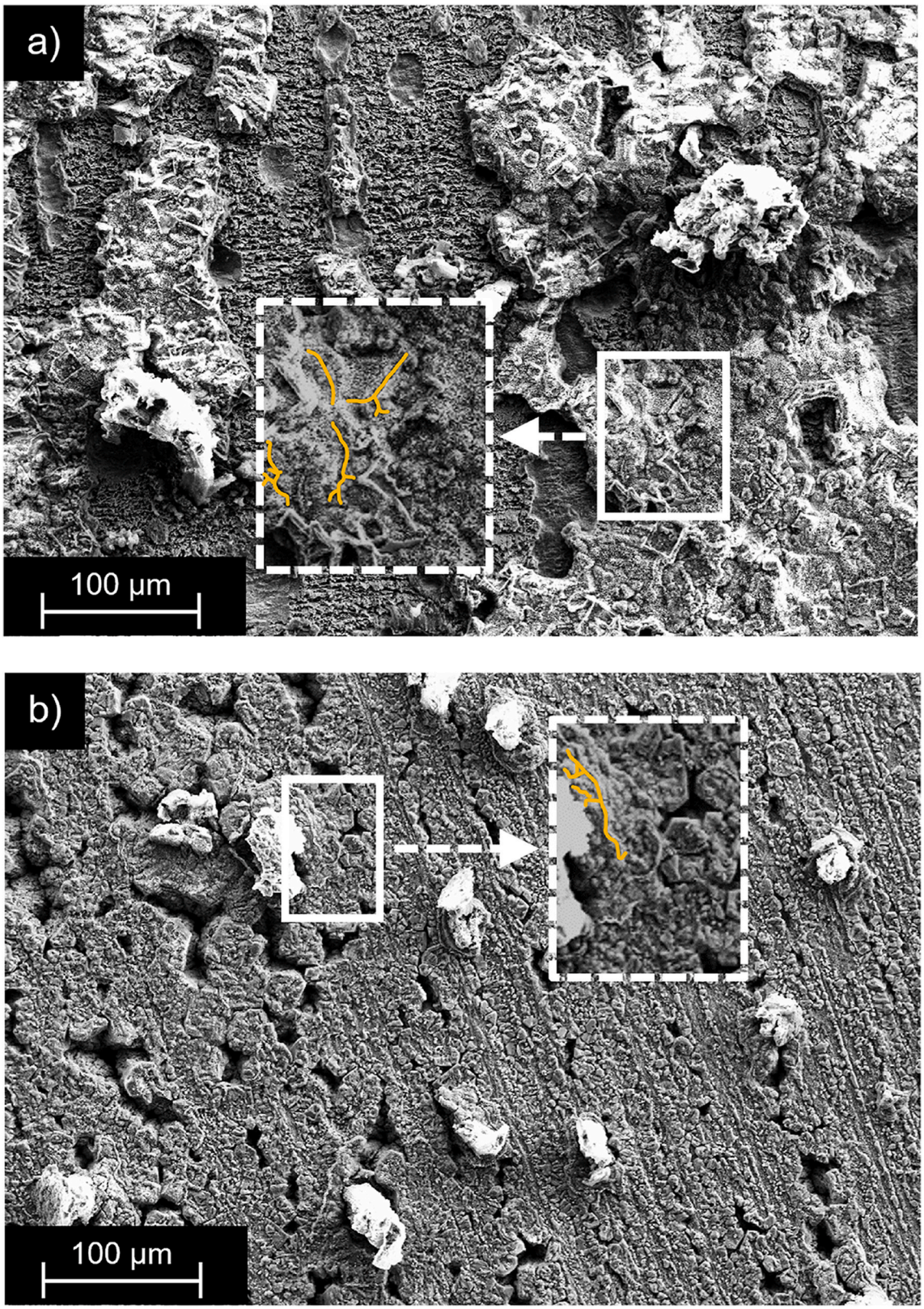

Fig. 11. SEM images of sanded X56 samples at magnification of 200X after a) 3 days and b) 14 days high-pressure experiments with H_2 and brine. In the images, the cracking patterns in the marked areas (continuous line) are highlighted in yellow within the magnification of these areas (dashed line). (For interpretation of the references to color in this figure legend, the reader is referred to the Web version of this article.)

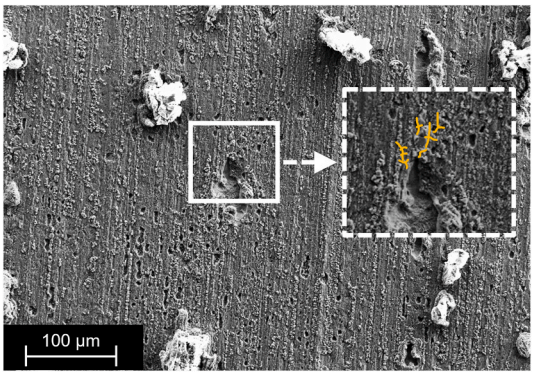

Fig. 12. SEM image of sanded X56 samples at magnification of 200X after 3 days high-pressure experiments with N_2 and brine. In the images, the cracking patterns in the marked areas (continuous line) are highlighted in yellow within the magnification of these areas (dashed line). (For interpretation of the references to color in this figure legend, the reader is referred to the Web version of this article.)

stability, possibly resulting in a reduction in material strength. Mechanical tests were not performed as part of this study, but they are useful for estimating the final effect on mechanical strength. Classical tensile tests cannot be performed on the samples considered due to the geometry and curvature of the pipe. Alternative characterization methods are required for this research, which will be performed in the form of micro tensile tests (M-TT) or small punch tests in following studies (SPT) [58].

Overall, the “H2ready” production process of X56 as well as the chemical composition seem to have a clear positive influence on preventing crack formation and establishing the formation of a passivating homogeneous oxide layer. As mentioned earlier, the X56 investigated in this study meets the strength requirements for a J55 classification, so the small deviation in strength should be negligible. Thus, the comparison of the two steels, J55 and X56, shows that from a scientific point of view, the “H2ready” X56 steel is more suitable for the typical application in an underground H_2 storage. However, the results might only provide an approximation to aging mechanisms under real H_2 salt cavern conditions. Steel samples from an existing H_2 underground storage are not available, yet. Nevertheless, for industrial realization, the study’s results can be considered, but a compromise between economic arguments and long-term durability always applies.

5. Conclusion

In this study, the casing steel API 5CT J55 and the pipeline steel API 5L X56 were tested on a laboratory scale as a potential option for the application in salt caverns for H_2 storage. The aim of the material selection was to compare a steel conventionally used for the storage of natural gas in caverns and a steel type of more recent development, for which the manufacturer is aiming for applications with compressed H_2.

Experiments were performed in high-pressure reactors under H_2 and N_2 atmospheres, respectively, applying an accelerated stress test by varying the temperature (−10 to 160 °C) with pressure change (90–150 bar) due to the autoclaved conditions. For separate as well as combined determination of the influence of H_2 and cavern conditions, dry and humid (water) conditions were tested in addition to the experiments with brine. To estimate the effects on the surface of the steel, longer experiments for 14 days were likewise performed in addition to the accelerated stress tests for 3 days. Characterization of the surface change was done using EDX and SEM. The focus was thus placed on the observation of the chemical corrosion effects (EDX) and the cracking patterns (SEM).

The analysis with EDX initially showed that for all conditions and gases corrosion of the two steels could be evidenced by an increase of oxygen on the surfaces, but there was a clear intensification of the effects for the brine conditions compared to the dry and humid ones. However, it should be emphasized that only for J55 an intensification of corrosion could be detected for H_2 exposed samples. The X56 steel showed less corrosion under the typical cavern conditions with brine and H_2, particularly in the long-term tests.

Not only the degree of oxide formation due to corrosion determined with EDX by the amounts of iron and oxygen on the surface indicate a higher resistance of X56, but also the SEM images reveal a homogeneous structured oxide layer for X56, which has a potential passivating effect. For J55, on the other hand, numerous local corrosion points were found, which in turn offer further paths of attack for hydrogen. The latter can additionally result from the formation of cracks on the surface of the steel. Through the evaluation of the SEM images, it could be demonstrated that for J55 a pronounced crack pattern developed under the conditions of the cavern (brine and H_2), especially after 14 days of stress test. In contrast, for X56 only minor cracking was found. It should be highlighted that for X56, again, no dependence on the gas (H_2 or N_2) and the conditions (dry, water, brine) could be determined concerning the crack formation.

As both steel types investigated, J55 and X56, have a similar classification and thus comparable material properties (material strength), the differences in the results are probably attributable in particular to the "H2ready" production route of X56. In addition to the aim of grain refinement and homogenization of the material, reduced phosphorus and sulfur contents are used in the alloy, resulting in fewer impurities and thus points of attack for hydrogen atoms. The SEM investigations carried out for J55 and X56 confirm this microstructure for X56 with finer grains than for J55.

In conclusion, the X56 steel displayed slight cracking and corrosion in the tests carried out in this study, but no significant intensification under typical cavern conditions with brine was observed. A distinct influence of the H_2 cannot be determined. From the comparative approach with SEM images and the interpretation of the identified trends from the EDX results it can be concluded that, from a scientific point of view, the "H2ready" X56 appears to be qualified for an underground application in the salt cavern with H_2 than the conventionally used J55 casing steel.

Funding

This work was supported by the project HyCavMobil, funded by the German Federal Ministry for Digital and Transport (BMDV) under grant no. 03B10902B within the National Innovation Programme for Hydrogen and Fuel Cell Technology (NIP 2), coordinated by NOW GmbH (National Organization Hydrogen and Fuel Cell Technology).

Declaration of competing interest

The authors declare that they have no known competing financial interests or personal relationships that could have appeared to influence the work reported in this paper.

References

[1] Sun YS, Zhao ZX, Yang M, Jia DQ, Pei W, Xu B. Overview of energy storage in renewable energy power fluctuation mitigation. Csee J Power Energy 2020;6:160–73.
[2] Pramuanjaroenkij A, Kakac S. The fuel cell electric vehicles: the highlight review. Int J Hydrogen Energy 2023;48:9401–25.
[3] Hwang J, Maharjan K, Cho H. A review of hydrogen utilization in power generation and transportation sectors: achievements and future challenges. Int J Hydrogen Energy 2023;48:28629–48.
[4] Samsun RC, Rex M, Antoni L, Stolten D. Deployment of fuel cell vehicles and hydrogen refueling station infrastructure: a global overview and perspectives. Energies 2022;15.
[5] Ball M, Wietschel M. The future of hydrogen – opportunities and challenges. Int J Hydrogen Energy 2009;34:615–27.

[6] Kurrer C. In: STOA) SFU, editor. The potential of hydrogen for decarbonising steel production. EPRS | European Parliamentary Research Service; 2020.
[7] Neuwirth M, Fleiter T, Manz P, Hofmann R. The future potential hydrogen demand in energy-intensive industries-a site-specific approach applied to Germany. Energy Convers Manag 2022:252.
[8] Liu WG, Zuo HB, Wang JS, Xue QG, Ren BL, Yang F, et al. The production and application of hydrogen in steel industry. Int J Hydrogen Energy 2021;46: 10548–69.
[9] Otto A, Robinius M, Grube T, Schiebahn S, Praktiknjo A, Stolten D. Power-to-Steel: reducing CO2 through the integration of renewable energy and hydrogen into the German steel industry. Energies 2017;10.
[10] Caglayan DG, Weber N, Heinrichs HU, Linssen J, Robinius M, Kukla PA, et al. Technical potential of salt caverns for hydrogen storage in Europe. Int J Hydrogen Energy 2020;45:6793–805.
[11] Liu W, Zhang ZX, Chen J, Jiang DY, Wei F, Fan JY, et al. Feasibility evaluation of large-scale underground hydrogen storage in bedded salt rocks of China: a case study in Jiangsu province. Energy 2020:198.
[12] Abreu JF, Costa AM, Costa PVM, Miranda ACO, Zheng ZY, Wang PF, et al. Large-scale storage of hydrogen in salt caverns for carbon reduction. Int J Hydrogen Energy 2023;48:14348–62.
[13] Williams JDO, Williamson JP, Parkes D, Evans DJ, Kirk KL, Sunny N, et al. Does the United Kingdom have sufficient geological storage capacity to support a hydrogen economy? Estimating the salt cavern storage potential of bedded halite formations. J Energy Storage 2022;53.
[14] Thiyagarajan SR, Emadi H, Hussain A, Patange P, Watson M. A comprehensive review of the mechanisms and efficiency of underground hydrogen storage. J Energy Storage 2022:51.
[15] Institute AP. Casing and tubing - API specification 5CT. Washington, D. C.: API Publishing Services; 2018.
[16] Cheng SX, Zhao XH, Fu AQ, Li DJ, Yin CX, Feng YR. Corrosion behavior of J55 and N80 carbon steels in simulated formation water under different CO2 partial pressures. Coatings 2022;12.
[17] Lin F, Xu M, Mu Y, Wang L. Experimental studies on corrosion behaviors of casing steel N80 in high salinity of brine. Adv Mater Res 2014;1081:205–9.
[18] Boersheim E, Reitenbach V, Albrecht D, Pudlo D, Ganzer L. Experimental investigation of integrity issues of UGS containing hydrogen. In: SPE europec featured at 81st EAGE conference and exhibition; 2019.
[19] Trautmann A, Mori G, Oberndorfer M, Bauer S, Holzer C, Dittmann C. Hydrogen uptake and embrittlement of carbon steels in various environments. Materials 2020;13.
[20] Institute AP. Line pipe - API specification 5L. Washington, D. C.: API Publishing Services; 2018.
[21] Mohtadi-Bonab MA, Szpunar JA, Basu R, Eskandari M. The mechanism of failure by hydrogen induced cracking in an acidic environment for API 5L X70 pipeline steel. Int J Hydrogen Energy 2015;40:1096–107.
[22] Bae DS, Sung CE, Bang HJ, Lee SP, Lee JK, Son IS, et al. Effect of highly pressurized hydrogen gas charging on the hydrogen embrittlement of API X70 steel. Met Mater Int 2014;20:653–8.
[23] Haq AJ, Muzaka K, Dunne DP, Calka A, Pereloma EV. Effect of microstructure and composition on hydrogen permeation in X70 pipeline steels. Int J Hydrogen Energy 2013;38:2544–56.
[24] Hejazi D, Haq AJ, Yazdipour N, Dunne DP, Calka A, Barbaro F, et al. Effect of manganese content and microstructure on the susceptibility of X70 pipeline steel to hydrogen cracking. Mat Sci Eng a-Struct. 2012;551:40–9.
[25] Capelle J, Gilgert J, Dmytrakh I, Pluvinage G. Sensitivity of pipelines with steel API X52 to hydrogen embrittlement. Int J Hydrogen Energy 2008;33:7630–41.
[26] Boukortt H, Amara M, Meliani MH, Bouledroua O, Muthanna BGN, Suleiman RK, et al. Hydrogen embrittlement effect on the structural integrity of API 5L X52 steel pipeline. Int J Hydrogen Energy 2018;43:19615–24.
[27] Willett E. Hydrogen Induced Cracking of Electric Welded J55 Casing. CORROSION 2010 2010.
[28] Brauer HS Manuel, Wanzenberg Elke, Henel Marco, Huising Otto Jan. Energiewende mit Wasserstoffrohren "H2Ready" und Umstellung existierender Erdgasnetze. 3R Fachzeitschrift für sichere und effiziente Rohrleitungssysteme. 2020. p. 32–45.
[29] Golisch G, Genchev G, Wanzenberg E, Mentz J, Brauer H, Muthmann E, et al. Application of line pipe and hot induction bends in hydrogen gas. J Pipeline Sci Eng 2022;2:100067.
[30] Li HY, Niu RM, Li W, Lu HZ, Cairney J, Chen YS. Hydrogen in pipeline steels: recent advances in characterization and embrittlement mitigation. J Nat Gas Sci Eng 2022;105.
[31] Arniella V, Zafra A, Belzunce J, Rodriguez C. Comparative study of embrittlement of quenched and tempered steels in hydrogen environments. Int J Hydrogen Energy 2022;47:17056–68.
[32] Nagumo M. Fundamentals of hydrogen embrittlement. Springer Singapore; 2016.
[33] Sk M, Abdullah A, Qi J, Ko M, Ingham B, Laycock N, et al. The effects of Cr/Mo micro-alloying on the corrosion behavior of carbon steel in CO 2 -saturated (sweet) brine under hydrodynamic control. J Electrochem Soc 2018;165:C278–88.
[34] Chen ZJ, Chen X, Zhou TP. Microstructure and mechanical properties of J55ERW steel pipe processed by on-line spray water cooling, vol. 7. Metals-Basel; 2017.
[35] Xu TL, Wang W, Jiang HY, He GZ. Study on micro crack propagation mechanism of ferrite-pearlite gas transmission pipeline steel with lamellar structure. Sci Rep-UK 2022;12.
[36] Grssinger R, Keplinger F, Mehmood N, Espina-Hernandez JH, Araujo J, Eisenmenger C, et al. Magnetic and microstructural investigations of pipeline steels. IEEE T Manag 2008;44:3277–80.
[37] Clover D, Kinsella B, Pejcic B, De Marco R. The influence of microstructure on the corrosion rate of various carbon steels. J Appl Electrochem 2005;35:139–49.
[38] Kim YS, Kim JG. Corrosion behavior of pipeline carbon steel under different iron oxide deposits in the district heating system. Metals-Basel 2017;7.
[39] Elfergani H, Abdalla A. Effect of chloride concentration on the corrosion rate in carbon steel. The 2nd Libyan conference on chemistry and its applications, vol. 2. LCCA-; 2017.
[40] Committee A. Standard specification for pressure vessel plates, carbon steel, low- and intermediate-tensile strength. ASTM A285: ASTM International; 2017.
[41] Zhao XH, Sheng YX, Yin CX, Li GF, Han Y. Effects of Cl- concentration on corrosion behavior of carbon steel and super13cr steel in simulated oilfield environments. In: International conference on innovative material science and technology (IMST 2016). Atlantis Press; 2016. p. 332–9.
[42] Kasthuri Rajagopalan K. Effect of sodium chloride concentration on the corrosion of carbon steels and stainless steels in CO2 environment at atmospheric pressure under turbulent flow condition. NACE - International Corrosion Conference; 2014.
[43] Thomas S, Sundararajan G, White PD, Birbilis N. The effect of absorbed hydrogen on the corrosion of steels: review, discussion, and implications. Corrosion 2017;73: 426–36.
[44] Rozenak P, Eliezer D. Effects of aging after cathodic charging in austenitic stainless-steels. J Mater Sci 1984;19:3873–9.
[45] Li W, Cochell T, Manthiram A. Activation of aluminum as an effective reducing agent by pitting corrosion for wet-chemical synthesis. Sci Rep-UK 2013;3.
[46] Schaller RF, Thomas S, Birbilis N, Scully JR. Spatially resolved mapping of the relative concentration of dissolved hydrogen using the scanning electrochemical microscope. Electrochem Commun 2015;51:54–8.
[47] Modiano S, Carreno J, Fugivara CS, Torresi RM, Vivier V, Benedetti A, et al. Changes on iron electrode surface during hydrogen permeation in borate buffer solution. Electrochim Acta 2008;53:3670–9.
[48] Yu JG, Luo JL, Norton PR. Electrochemical investigation of the effects of hydrogen on the stability of the passive film on iron. Electrochim Acta 2002;47:1527–36.
[49] Thomas S, Ott N, Schaller RF, Yuwono JA, Volovitch P, Sundararajan G, et al. The effect of absorbed hydrogen on the dissolution of steel. Heliyon 2016;2:e00209.
[50] Pichler S, Bendo A, Mori G, Safyari M, Moshtaghi M. Inhibition of grain growth by pearlite improves hydrogen embrittlement susceptibility of the ultra-low carbon ferritic steel: the influence of H-assisted crack initiation and propagation mechanisms. J Mater Sci 2023;58:13460–75.
[51] Park C, Kang N, Liu S. Effect of grain size on the resistance to hydrogen embrittlement of API 2W Grade 60 steels using in situ slow-strain-rate testing. Corrosion Sci 2017;128:33–41.
[52] Chen L, Xiong XL, Tao X, Su YJ, Qiao LJ. Effect of dislocation cell walls on hydrogen adsorption, hydrogen trapping and hydrogen embrittlement resistance. Corrosion Sci 2020;166:108428. 2020;169.
[53] Sastri VS. Challenges in corrosion. John Wiley & Sons; 2015.
[54] Sotoodeh K. Chapter 5 - hydrogen sulfide corrosion. In: Sotoodeh K, editor. Case studies of material corrosion prevention for oil and gas valves. Gulf Professional Publishing; 2022. p. 191–225.
[55] Wasim M, Djukic MB, Ngo TD. Influence of hydrogen-enhanced plasticity and decohesion mechanisms of hydrogen embrittlement on the fracture resistance of steel. Eng Fail Anal 2021;123:105312.
[56] Carneiro RA, Ratnapuli RC, Lins VD. The influence of chemical composition and microstructure of API linepipe steels on hydrogen induced cracking and sulfide stress corrosion cracking. Mat Sci Eng a-Struct 2003;357:104–10.
[57] Jiang YF, Zhang B, Wang DY, Zhou Y, Wang JQ, Han EH, et al. Hydrogen-assisted fracture features of a high strength ferrite-pearlite steel. J Mater Sci Technol 2019; 35:1081–7.
[58] Konopik P, Farahnak P, Rund M, Prochazka R, Džugan J. Application of micro-tensile test for material characterization of mild steel DC01. Ubiquity Proceedings 2018:33.